Published in final edited form as:

J Mol Biol. 2020 January 17; 432(2): 410–426. doi:10.1016/j.jmb.2019.11.002.

Structural Basis of Protein Arginine Methyltransferase Activation by a Catalytically Dead Homolog (Prozyme)

Hideharu Hashimoto[1], **Lucie Kafková**[2], **Ashleigh Raczkowski**[3], **Kelsey D. Jordan**[3], **Laurie K. Read**[2], **Erik W. Debler**[1]

[1]Department of Biochemistry and Molecular Biology, Thomas Jefferson University, Philadelphia, PA 19107, USA

[2]Department of Microbiology and Immunology and Witebsky Center for Microbial Pathogenesis and Immunology, SUNY Buffalo, Buffalo, NY 14203, USA

[3]Simons Electron Microscopy Center, New York Structural Biology Center, New York, NY 10027, USA

Abstract

Prozymes are pseudoenzymes that stimulate the function of weakly active enzymes through complex formation. The major *Trypanosoma brucei* protein arginine methyltransferase, *Tb*PRMT1 enzyme (ENZ), requires *Tb*PRMT1 prozyme (PRO) to form an active heterotetrameric complex. Here we present the x-ray crystal structure of the *Tb*PRMT1 ENZ-Δ52PRO tetrameric complex with the cofactor product S-adenosyl-L-homocysteine (AdoHcy) at 2.4 Å resolution. The individual ENZ and PRO units adopt the highly-conserved PRMT domain architecture and form an antiparallel heterodimer that corresponds to the canonical homodimer observed in all previously reported PRMTs. In turn, two such heterodimers assemble into a tetramer both in the crystal and in solution with twofold rotational symmetry. ENZ is unstable in absence of PRO and incapable of forming a homodimer due to a steric clash of an ENZ-specific tyrosine within the dimerization arm, rationalizing why PRO is required to complement ENZ to form a PRMT dimer that is necessary, but not sufficient for PRMT activity. The PRO structure deviates from other, active PRMTs in that it lacks the conserved η2 3_{10}-helix within the Rossmann fold, abolishing co-factor binding. In addition to its chaperone function for ENZ, PRO substantially contributes to substrate binding. Heterotetramerization is required for catalysis, since heterodimeric ENZ-PRO mutants lack binding affinity and methyltransferase activity towards the substrate protein *Tb*RGG1. Together, we provide a structural basis for *Tb*PRMT1 ENZ activation by PRO heterotetramer formation, which is conserved across all kinetoplastids, and describe a chaperone function of the *Tb*PRMT1 prozyme, which represents a novel mode of PRMT regulation.

Graphical Abstarct

Correspondence to Erik W. Debler: Erik.Debler@jefferson.edu, Phone: +1-215-503-4596, Fax: +1-215-503-4100, 1020 Locust Street, JAH 411F, Philadelphia, PA 19107, USA.

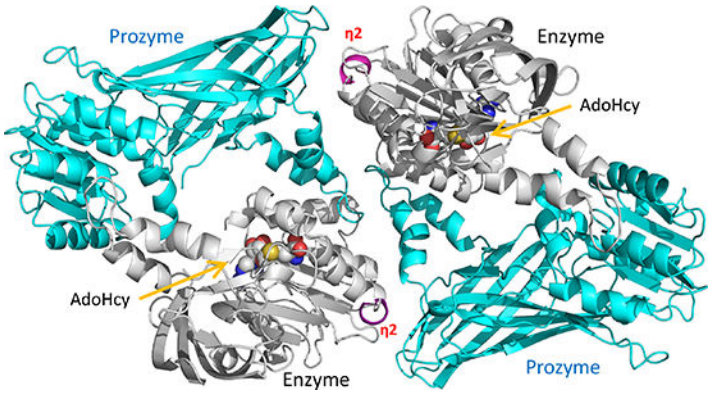

Keywords

PRMT1; pseudoenzyme; chaperone; *Trypanosoma brucei*; oligomerization

Introduction

Trypanosoma brucei is a protozoan parasite that can cause fatal sleeping sickness in humans and various animal diseases in Sub-Saharan Africa. An estimated 70 million people are at risk of infection [1]. African trypanosomes adopt two distinct replicative forms during their life cycle, the bloodstream form in the mammal and the procyclic form in the midgut of its insect vector, the tsetse fly [2]. Control of gene expression and life-cycle progression primarily takes place on the post-transcriptional level [3]. However, recent evidence points towards a role of chromatin proteins in this process as well [4]. Among the posttranslational modifications that impact gene expression and other cellular functions, arginine methylation is prevalent with at least 15% of the proteome being modified, including proteins involved in a wide spectrum of processes such as RNA processing, DNA repair, metabolism, and protein trafficking [5, 6]. Arginine methylation is catalyzed by S-adenosyl-L-methionine (AdoMet)-dependent protein arginine (R) methyltransferases (PRMTs) [7]. Type I PRMTs (PRMT1, 2, 3, 4, 6, and 8) generate monomethyl arginine (MMA) and asymmetric dimethyl arginine (ADMA); type II PRMTs (PRMT5 and 9) generate MMA and symmetric dimethyl arginine (SDMA); and type III PRMTs (PRMT7) only produce MMA [8, 9]. Their product specificities are restricted by the size and architecture of their active-site pockets [9–11].

*Tb*PRMT1 enzyme (ENZ) is the predominant type I PRMT1 in *T. brucei* that produces MMA and ADMA [12–14]. It contributes to parasite virulence, metabolic regulation, and nutritional stress response [15]. RGG/RG motifs are often the target of asymmetric arginine dimethylation in substrates, including the *Tb*PRMT1 substrates *Tb*RBP16 and *Tb*RGG1 [16]. The *Tb*PRMT1 ENZ shares 51% identical residues with type I human and rat PRMT1 [13, 17], and 41% identical residues with type I rat PRMT3 [18]. The PRMT structures suggest that the PRMT fold and the catalytic mechanism are conserved and that at least dimerization of the PRMT cores is required for AdoMet binding and catalysis [17–19]. Human, rat, and yeast PRMT1s are homo-oligomeric complexes with molecular weights of 300–400 kDa in solution [19–21], while rat PRMT3 exists in a monomer-dimer equilibrium in the cell with an activity of 0.3% with respect to rat PRMT1 [18, 22]. By contrast,

*Tb*PRMT1 ENZ forms a stable heterotetrameric complex with a catalytically inert *Tb*PRMT1 prozyme (PRO), which was previously termed *Tb*PRMT3 [14]. The methyltransferase activity of *Tb*PRMT1 ENZ by itself is not detectable, but catalytically inert *Tb*PRMT1 PRO is necessary and sufficient to enable *Tb*PRMT1 activity. The mRNA level and protein amount of *Tb*PRMT1 ENZ are constant in both the procyclic and the bloodstream form [23–26]. The protein expression levels of ENZ and PRO are strongly synchronized and interdependent [27]: Repression of *Tb*PRMT1 PRO mRNA reduces the *Tb*PRMT1 ENZ protein level, although the *Tb*PRMT1 ENZ mRNA level remained unchanged [13, 27]. We therefore proposed that the amount of catalytically active *Tb*PRMT1 ENZ is regulated by the catalytically inert *Tb*PRMT1 PRO [14].

In addition to *Tb*PRMT1, three other enzymatic activities activated by prozymes have been discovered in *T. brucei* to date: AdoMet decarboxylase (*Tb*AdoMetDC), *Tb*RNase III endonucleases within the editosome, and deoxyhypusine synthase (*Tb*DHS) in the polyamine synthesis pathway [14, 28–32]. Prozymes are a subgroup of pseudoenzymes, which are estimated to represent ~10% of the human proteome and are thought to serve as regulators of enzymes [33, 34]. So far, six modes of pseudoenzyme function have been proposed [34]. The *Tb*AdoMetDC enzyme homodimer is inactive due to blockage of the active-site pocket by an N-terminal fragment [29]. The *Tb*AdoMetDC prozyme allosterically unblocks the active site in the catalytically active enzyme-prozyme heterodimer, facilitating enzymatic activity [29]. As for *Tb*RNase III endonucleases within the editosome, three prozymes adopt a chaperone function to form enzymatically competent heterodimeric complexes, but their detailed mechanism of action is presently unclear [32].

*Tb*PRMT1 ENZ and catalytically inactive *Tb*PRMT1 PRO share several conserved features, including the Rossmann fold and motifs I and II (highlighted in bold in Fig. 1), albeit with a lower sequence identity (27%, 82 residues of 304) and similarity (44%, 136 residues of 304) than with human or rat PRMT1 [35]. A striking difference refers to conserved AdoMet binding residues [36, 37], many of which are lacking in *Tb*PRMT1 PRO (Fig. 1). AdoMet crosslink experiments demonstrated that *Tb*PRMT1 ENZ but not *Tb*PRMT1 PRO binds AdoMet, consistent with the notion that PRO is a catalytically inactive enzyme [14].

In order to elucidate the structural basis of enzyme activation by prozyme in *Tb*PRMT1, we determined the crystal structure of the *Tb*PRMT1 ENZ-PRO complex, analyzed its oligomeric state in solution, and performed substrate binding and methyltransferase assays of wild-type and mutant *Tb*PRMT1 ENZ and PRO species. Our results reveal that *Tb*PRMT1 PRO is required for *Tb*PRMT1 ENZ stability, that the heterotetrameric architecture of the *Tb*PRMT1 ENZ-PRO complex is necessary for substrate binding and catalytic activity, and that the features of the *Tb*PRMT1 ENZ-PRO complex are conserved among kinetoplastids, implying a similar mode of PRMT1 regulation in these organisms.

Results

*Tb*PRMT1 ENZ-PRO forms a heterotetrameric complex

*Tb*PRMT1 ENZ-PRO from procyclic-form cells as well as the recombinantly expressed complex in *Escherichia coli* forms a heterotetramer as deduced from ultracentrifugation, size

exclusion chromatography, and multiangle light scattering coupled to size exclusion chromatography (SEC-MALS) [14]. Because wild-type *Tb*PRMT1 ENZ was insoluble or unstable [14] (Table 1), the wild-type *Tb*PRMT1 ENZ (residues 1–345) and hexa-histidine-tagged wild-type *Tb*PRMT1 PRO (residues 1–389) were co-expressed in *E. coli* using a pETDuet vector system (Novagen) and purified from the soluble fraction, followed by His-tag removal. According to SEC-MALS, the size of this complex was about 164 kDa, which corresponds to a heterotetrameric complex (theoretical molecular weight of 163.2 kDa), as previously described (Table 1) [14]. The heterotetrameric complex was further confirmed by small angle x-ray scattering coupled to SEC (SEC-SAXS) (Fig. 2a) and by negative-stain electron microscopy (EM) (Fig. 2b). In detail, the SEC-SAXS profile yielded a single peak with a constant radius of gyration across the peak (~43.0 Å) (Fig. 2a). Based on the volume of correlation (V_c) of this peak [38], a molecular weight of 187 kDa was estimated (Table 2). The Guinier and Kratky plots revealed that the complex was monodisperse and fully folded (Fig. 2a). The *Tb*PRMT1 ENZ-PRO complex visualized by negative-stain EM showed four distinct globular masses symmetrically arranged at the vertices of a rhomboid structure in the most predominant 2D class average (Fig. 2b). The complex measures about 140 Å in its longest dimension, which fits the maximum distance of 143 Å obtained in a pair-distance distribution by SEC-SAXS (Fig. 2a). Finally, a stoichiometry of 1:1 was obtained for the *Tb*PRMT1 heterotetramer with a Maltose Binding Protein (MBP)-fused *Tb*RGG1 substrate by isothermal titration calorimetry (ITC) (Fig. 2c and Table 1) [14]. Collectively, these data demonstrate that the *Tb*PRMT1 complex forms a rigid heterotetrameric unit in solution.

The *Tb*PRMT1 PRO N-terminus contributes to substrate recognition

Previous studies have shown that all PRMTs contain a highly conserved core domain comprising ~310 residues [8] and that the N-terminal region of PRMTs is often flexible and involved in substrate recognition [39, 40]. Among kinetoplastids, the N-terminal regions of putative PRMT1 ENZ and PRO have highly diverged (Fig. S1 and S2). Therefore, we examined the role of the N-terminal residues of *Tb*PRMT1 PRO and ENZ. Limited proteolysis on the full-length proteins identified a stable, N-terminally truncated *Tb*PRMT1 PRO fragment spanning residues 53–389, referred to as *Tb*PRMT1 Δ52PRO, while *Tb*PRMT1 ENZ remained intact under the conditions tested. The *Tb*PRMT1 Δ52PRO fragment was then co-expressed with full-length *Tb*PRMT1 ENZ. SEC-MALS, SEC-SAXS, and SEC alone confirmed that the *Tb*PRMT1 ENZ-Δ52PRO complex still formed a tetrameric complex (Fig. S3a and Tables 1 and 2). However, its binding affinity for MBP-*Tb*RGG1 was abolished (Fig. S3b), consistent with methyltransferase inactivity, even in complex with full-length *Tb*PRMT1 ENZ (Table 1). These data suggest that the N-terminus of *Tb*PRMT1 PRO is essential for substrate binding, while the N-terminal region of *Tb*PRMT1 ENZ is not sufficient for that. When we measured the methyltransferase activities and MBP-*Tb*RGG1 protein binding affinities of a series of N-terminal *Tb*PRMT1 PRO deletion mutants in complex with full-length wild-type *Tb*PRMT1 ENZ, we found that the first ~40 N-terminal, non-conserved residues of *Tb*PRMT1 PRO are dispensable for methyltransferase activity (Table 1 and Fig. S2). These data imply that the conserved N-terminal region between residues 41 and 52 of *Tb*PRMT1 PRO is critical for substrate recognition, whereas the N-terminal residues 1–15 of ENZ are not sufficient for substrate binding, consistent with its non-conserved nature among kinetoplastids (Fig. S1).

*Tb*PRMT1 ENZ and PRO form heterodimers that assemble into a heterotetramer

In order to obtain mechanistic insights into *Tb*PRMT1 ENZ activation by *Tb*PRMT1 PRO at atomic resolution, we crystallized the stable *Tb*PRMT1 ENZ-Δ52PRO complex with the methylation cofactor product AdoHcy and solved the structure at 2.4 Å resolution from a seleno-methionine derivatized crystal using the single anomalous dispersion (SAD) phasing technique (Supplemental Table S1). Two *Tb*PRMT1 ENZ (shown in gray) and two *Tb*PRMT1 Δ52PRO (shown in cyan) molecules form the asymmetric unit (Fig. 3a). No electron density of the *Tb*PRMT1 ENZ residues 1–20, the *Tb*PRMT1 ENZ loop region between β9-β10 strands (residues 241–250), and *Tb*PRMT1 Δ52PRO residues 53–70 was observed. Consistent with our previous biochemical finding [14], AdoHcy was only bound to *Tb*PRMT1 ENZ (Fig. 3a). Notably, one *Tb*PRMT1 ENZ and one *Tb*PRMT1 Δ52PRO molecule form a canonical PRMT ring-like dimeric structure that has been observed in all other, homodimeric PRMTs thus far [17–19, 41] (Fig. 3b). In turn, two *Tb*PRMT1 ENZ-Δ52PRO heterodimers touch each other side by side, exhibiting a 2-fold non-crystallographic symmetry (Fig. 3a). The two dimers are highly similar with a root-mean-square deviation (rmsd) of only 0.6 Å when comparing 637 pairs of Cα atoms. The dimensions of the *Tb*PRMT1 ENZ-Δ52PRO heterotetrameric complex are 131 Å × 70 Å × 78 Å (Fig. 3a). Importantly, the molecular size and shape of the crystal structure are in good agreement with the results of SEC-MALS (Table 1), SEC-SAXS (Supplemental Fig. S3a, Fig. 2a, and Table 2), and electron microscopy (Fig. 2b), therefore corroborating the tetrameric form in solution, which is further confirmed by comparing the calculated radii of gyration of the *Tb*PRMT1 ENZ-Δ52PRO heterotetramer and heterodimer (39 Å and 28 Å, respectively) with the experimental radius of gyration (41Å) [42].

*Tb*PRMT1 ENZ adopts the canonical PRMT fold and features a type I active-site architecture

*Tb*PRMT1 ENZ harbors seven α-helices, six 3_{10}-helices, and 15 β-strands (Figs. 1, 3c, and 3e). The two *Tb*PRMT1 ENZ molecules within the asymmetric unit are highly similar (rmsd of 0.4 Å, comparing 318 pairs of Cα atoms). The overall monomeric structure of *Tb*PRMT1 ENZ strongly resembles the monomeric class I PRMT core domain structure of rat PRMT1, rat PRMT3, mouse CARM1 (PRMT4), and yeast RMT1 (Supplemental Table S2), sharing an identical topology with the rat PRMT1 core domain (Fig. 3e and Supplemental Fig. S4) [17–19, 41]. Like other PRMTs, *Tb*PRMT1 ENZ contains the four highly conserved modules of PRMTs: an N-terminal helical extension (residues 20–33 in red), a Rossmann fold (residues 34–157 in green), a dimerization arm (residues 168–199 in purple), and a β-barrel domain (residues 158–345 in orange) (Figs. 3b, 3c, and Supplemental Fig. S4). The electron density of the co-factor product AdoHcy is clearly observed in both *Tb*PRMT1 ENZ molecules (Figs. 3a and 3h). AdoHcy interacts with residues that are highly conserved among human PRMT1, rat PRMT1, and *Tb*PRMT1 ENZ for AdoMet binding [17, 18, 36]: Tyr22, His28, Arg37, Asp83, Cys84, Glu112, Glu126, Met137, Thr140, the main chain of Gly63 and Val111, and Asp59 via two water molecules (Fig. 3h). The *Tb*PRMT1 ENZ active site possesses the previously described PRMT type I features [9–11]: An open subregion A is adjacent to the double E-loop, while subregion B towards the conserved THW loop is sterically more restricted, which enables conversion to mono- and asymmetric dimethyl arginine, but not to symmetric dimethylarginine (Supplemental Fig. S5). The

distances between atoms of conserved *Tb*PRMT1 ENZ residues and of the sulfur atom of AdoHcy recapitulate the type I enzyme active-site architecture and provide a structural basis for *Tb*PRMT1 ENZ product specificity [14].

Lack of the η2 3_{10}-helix is a unique feature of the *Tb*PRMT1 PRO core domain that twists its Rossmann fold

The two *Tb*PRMT1 Δ52PRO molecules (cyan in Fig. 3a) within the asymmetric unit superimpose closely (rmsd of 0.4 Å, comparing 319 pairs of Cα atoms) and harbor the four canonical PRMT modules: an N-terminal helical extension (residues 71–80 in red), a Rossmann fold (residues 81–202 in green), a dimerization arm (residues 213–244 in purple), and a β-barrel domain (residues 203–389 in orange) (Figs. 3b and 3d). While the monomeric structures of *Tb*PRMT1 ENZ and Δ52PRO are relatively similar (Fig. 3g, rmsd of 2.1 Å, comparing 293 pairs of Cα atoms), the topology of *Tb*PRMT1 Δ52PRO bears a few marked differences with respect to *Tb*PRMT1 ENZ and other PRMT1s (Figs. 3e and 3f) [17–19, 41]. Within the Rossmann fold, *Tb*PRMT1 PRO lacks the η2 3_{10}-helix between the α2 helix and β1 strand, and has an extra η4 3_{10}-helix between the η3 3_{10}-helix and β4 strand (Figs. 1 and 3f). Importantly, the η2 3_{10}-helix is highly conserved among active enzymes (Supplemental Fig. S6) [8]. As a result of the lacking η2 3_{10}-helix, the α2, α3 and, α4 helices within the *Tb*PRMT1 PRO Rossmann fold are tilted by 10–20°, whereas the β sheets of the *Tb*PRMT1 ENZ and PRO Rossmann folds align well (Fig. 3g). In turn, these observed differences in the secondary structure elements of *Tb*PRMT1 PRO twist and hence affect the dimerization interface, compromising cofactor AdoMet binding and providing a structural basis for *Tb*PRMT1 PRO inactivity.

*Tb*PRMT1 PRO is required for dimerization and ENZ stability

The η1 3_{10}-helix and the α1 and α2 helices contribute to AdoMet binding (Fig. 3h) and dimerization of PRMTs (Fig. 3b) [8]. The total buried dimerization surface area between *Tb*PRMT1 ENZ and PRO is ~1,600 $Å^2$, which is similar to that of other, homodimeric PRMTs. Since dimerization arm mutants that lead to monomeric PRMTs do not have methyltransferase activity [10, 17, 19], dimerization of PRMTs is required for activity [9, 10, 17–19, 39, 41, 43]. As we previously reported, *Tb*PRMT1 ENZ expressed by itself is an unstable protein that requires *Tb*PRMT1 PRO to form a stable, catalytically active complex [14]. *Tb*PRMT1 PRO, on the other hand, can be expressed by itself, albeit at a reduced amount, indicating decreased stability, and forms a homodimer [14]. Thus, the protein amount of folded *Tb*PRMT1 ENZ is limited and hence may be regulated by *Tb*PRMT1 PRO *in vivo* [14, 27]. As the molecular surface of the monomeric *Tb*PRMT1 ENZ structure displays highly hydrophobic patches, covering these hydrophobic regions via dimerization with *Tb*PRMT1 PRO is a likely mechanism to stabilize the *Tb*PRMT1 ENZ protein. Particularly the dimerization arm of *Tb*PRMT1 ENZ is highly hydrophobic and dominated by aromatic residues (Fig. 4a). In detail, the hydrophobic residues Ile179, Trp180, Val183, Ile186, Phe188, Tyr190, Phe191, and Leu194 of the ENZ dimerization arm contact the hydrophobic residues Ile72, Leu76, Ile79, Leu85, Met107, Leu109, Ile113, Ile130, Ala133, and Val137 on the η1 3_{10}-helix, α1, α2, and α3 helices of *Tb*PRMT1 PRO (Fig. 4c). Similarly, the surface of the *Tb*PRMT1 PRO dimerization arm is hydrophobic. The *Tb*PRMT1 PRO residues Thr221, Phe224, Trp225, Val228, Tyr229, Phe231, Met233,

Pro235, Met236, Leu239, and Val240 contact the hydrophobic *Tb*PRMT1 ENZ residues Tyr25, Met29, Lys33, Cys35, Thr38, Thr39, Arg42, Trp46, Thr64, Ile66, Phe70, Val87, Gln90, Ile94 and Phe100 on the η1 3_{10}-helix, α1, α2, and α3 helices (Fig. 4b). Upon dimerization of *Tb*PRMT1 ENZ and PRO, the hydrophobic patches of the η1 3_{10}-helix and α1 helix in *Tb*PRMT1 ENZ become buried, leading to ENZ stabilization.

The two dimerization arms of *Tb*PRMT1 ENZ and PRO are structurally highly similar (rmsd of 0.7 Å, comparing 124 pairs of Cα atoms). When we generate homodimeric models of *Tb*PRMT1 ENZ and PRO, respectively, we observe that *Tb*PRMT1 PRO can indeed form homodimers without any severe steric clashes (Fig. 4d), while Tyr190 of *Tb*PRMT1 ENZ, corresponding to Pro235 of *Tb*PRMT1 PRO, clearly clashes with the side chains of Gln90, Glu93, and Ile94 on the α4 helix of *Tb*PRMT1 ENZ (Fig. 4e). Consequently, *Tb*PRMT1 ENZ is predicted to be unable to form a homodimer due to steric clashes and requires *Tb*PRMT1 PRO to engage into a stable *Tb*PRMT1 ENZ-PRO complex.

The *Tb*PRMT1 heterotetrameric assembly is required for substrate binding and catalytic activity

Human and rat PRMT1 predominantly form oligomeric structures [17, 19–21], which are the active species *in vivo* [44]. PRMT3 exists in a monomer-dimer equilibrium in solution [18, 22]. However, PRMT3 crystal structures revealed the canonical dimeric arrangement, consistent with the notion that PRMT dimerization is necessary for catalytic activity [17–19]. *Tb*PRMT1 ENZ and PRO form a stable heterotetramer (Figs. 2 and 3a) [14] that binds one substrate molecule (Fig. 2c). The interface between two heterodimers amounts to ~950 $Å^2$ and is dominated by van der Waals' contacts; Tyr50 of *Tb*PRMT1 ENZ interacts with hydrophobic residues Val375 and Val376 of *Tb*PRMT1 PRO, His270 of *Tb*PRMT1 ENZ interacts with residues Asp292, Thr293, Thr294, Pro340, Leu341, and Val375 of PRO, Tyr215 of *Tb*PRMT1 PRO interact with residues Asp43, Trp46, and Arg47 of *Tb*PRMT1 ENZ, and Met219 of *Tb*PRMT1 PRO interacts with Trp46 of *Tb*PRMT1 ENZ (Fig. 5). We mutated various key dimer-dimer surface residues to alanine in order to test whether they break down the tetramer into dimers, and evaluated the size of the resulting mutants using SEC, SEC-MALS, SEC-SAXS, and EM (Fig. 6, Tables 2 and 3). Indeed, the *Tb*PRMT1 ENZ triple mutant W46A/R47A/Y50A, the *Tb*PRMT1 ENZ double mutant Y50A/H270A, the *Tb*PRMT1 PRO double mutants Y215A/M219A, Y215A/E223A, Y215A/K232A, Y215A/T294A, as well as the *Tb*PRMT1 PRO triple mutant Y215A/M219A/E223A all disrupt the tetrameric complex and form a stable heterodimer. Moreover, the combination of a single mutation in each protein, H270A in *Tb*PRMT1 ENZ and Y215A in *Tb*PRMT1 PRO, disrupted the tetramer as well (Tables 2 and 3). In contrast to the rhomboid shape of the wild-type, negative-stain EM analysis of a mutant revealed a square-shaped structure, consistent in shape and size with an *Tb*PRMT1 ENZ-PRO heterodimeric unit (Figs. 3b and 6b). Extensive SEC-SAXS data obtained from these mutants confirm the substantially smaller size of the heterodimer with respect to the heterotetrameric wild-type structure (Fig. 6a, Table 2). These solution studies verify the dimer-dimer interface observed in the crystal structure. Importantly, ITC binding and methyltransferase assays showed that none of the dimeric mutants bound MBP-*Tb*RGG1 and did not possess any detectable methyltransferase activity (Fig. 6c and Table 3). On the other hand, the single mutations K73A, W64A, R47A,

Y50A, and H270A in *Tb*PRMT1 ENZ, the double alanine mutant H270A/E271A in *Tb*PRMT1 ENZ and single mutations Y215A and K232A in *Tb*PRMT1 PRO retained the tetrameric assembly and methylate the substrate as the wild-type complex (Table 3). We conclude that the determined *Tb*PRMT1 ENZ-PRO heterotetramer structure is the biological functional unit both *in vitro* and *in vivo* [14], and that heterotetramer assembly is required for substrate binding and methyltransferase activity.

Discussion

Catalytically inert pseudoenzymes are abundant in the proteome and perform diverse functions, serving as scaffold proteins [45], modulators of enzyme activity and signaling pathway components [30], or competitors of active paralogs for substrate(s) [34]. Prozymes are a subgroup of pseudoenzymes that specifically stimulate an otherwise inactive enzyme by complex formation. Here, we describe a chaperone function of the *Tb*PRMT1 prozyme (PRO) in complex with the *Tb*PRMT1 enzyme (ENZ) in *T. brucei*. Structural and functional analyses reveal distinct structural features that set *Tb*PRMT1 PRO apart from its active counterpart *Tb*PRMT1 ENZ and elucidate the mechanism of *Tb*PRMT1 ENZ activation by *Tb*PRMT1 PRO through oligomerization.

Sequence analysis alone had already indicated that *Tb*PRMT1 PRO was lacking conserved residues that are critical for catalysis and methyl donor (AdoMet) binding and hence provided evidence that *Tb*PRMT1 PRO would catalytically be inactive [14]. Indeed, the crystal structure of the *Tb*PRMT1 ENZ-PRO complex showed that the cofactor product was only bound to *Tb*PRMT1 ENZ, in agreement with an AdoMet crosslink experiment (Fig. 3h) [14]. However, our structural analysis revealed further marked differences on the secondary-structure level of *Tb*PRMT1 PRO with respect to *Tb*PRMT1 ENZ (Fig. 1), most notably the lack of the η2 3_{10}-helix in the Rossmann fold of PRO, which affect its tertiary structure (Fig. 3g) and which are ultimately critical for its catalytic inactivity. The lack of the η2 3_{10}-helix results in a tilt of several adjacent α-helices, which in turn affect dimerization and abolish cofactor binding in the prozyme (Fig. 3g).

While *Tb*PRMT1 ENZ possesses all essential residues and secondary structure elements for cofactor AdoMet binding and catalysis (Figs. 1 and 3h), *Tb*PRMT1 ENZ itself is unstable in solution in the absence of *Tb*PRMT1 PRO and hence incapable of catalysis [27]. *Tb*PRMT1 ENZ features highly hydrophobic patches in the dimerization arm that are thermodynamically unfavorable if exposed to solvent [46]. While hydrophobic patches are also found in other PRMTs, homodimerization covers these hydrophobic patches to stabilize the active enzymes [8, 17–19]. By contrast, *Tb*PRMT1 ENZ homodimerization is sterically prevented, specifically by Tyr190 within the dimerization arm of *Tb*PRMT1 ENZ (Fig. 4e). In mammalian and yeast class I PRMTs, as well as in *Tb*PRMT1 PRO, the corresponding residue is mostly a cysteine or a proline, thus facilitating formation of a stable homodimer [14, 17–19] (Fig. 4a). However, we note that the Tyr190 mutation to Cys or Pro was not sufficient to form a homodimeric enzyme complex (data not shown), suggesting that homodimerization does not depend on a single residue.

Higher-order oligomerization beyond the homodimer is well established in PRMTs. For example, PRMT1s from various organisms form a hexamer in solution [17, 19–21]. While the oligomerization of mammalian and yeast PRMT1s is dependent on PRMT concentration [17], we did not detect such a dependence for the *Tb*PRMT1 complex, as it always remained tetrameric under different protein concentrations (Supplemental Fig. S7). Dimerization is required for AdoMet binding in PRMTs [17–19], and even higher oligomerization of human PRMT1 is required for its catalysis *in vivo* [44]. As we demonstrated here, substrate binding and methyltransferase activities are essentially abolished in the stable *Tb*PRMT1 ENZ-PRO dimeric complex mutants with respect to the wild-type tetrameric complex (Table 2). We conclude that oligomers beyond the dimer may generally constitute the active species of PRMT1s, with dimerization not being sufficient for its activities *in vitro* and/or *in vivo*.

Although the *Tb*PRMT1 ENZ-PRO heterotetramer possesses two active sites, only one MBP-*Tb*RGG1 substrate molecule is bound to the tetramer (Fig. 2c). In principle, an allosteric mechanism between the two heterodimers could explain this finding, whereby substrate binding to one heterodimer would induce changes in the other dimer that would prevent further substrate binding. Alternatively, a tetramer could provide a unique composite interaction surface not present in the heterodimer. Our ITC experiments show that substrate binding is abolished in heterodimer mutants (Table 2), supporting the latter mechanism. We cannot exclude though that both *Tb*PRMT1 ENZ-PRO heterodimers of a tetramer may independently and in parallel be engaged in the methylation of other substrate proteins or even *Tb*RGG1 without the bulky MBP fusion partner [13]. However, attempts to remove the MBP fusion partner from *Tb*RGG1 have not yielded stable *Tb*RGG1.

The concept that *Tb*PRMT1 PRO is necessary to form a stable, catalytically active PRMT heterodimer with *Tb*PRMT1 ENZ has important implications for regulation. In essence, the activity of *Tb*PRMT1 ENZ would be regulated by the protein amount of *Tb*PRMT1 PRO. As the knockdown of *Tb*PRMT1 PRO has shown, its mRNA reduction did not affect the mRNA amount of *Tb*PRMT1 ENZ, but affected the protein amount of *Tb*PRMT1 ENZ [27]. Unlike all previously reported PRMTs, *Tb*PRMT1 ENZ is unstable on its own because it cannot form a homodimer, in part due to Tyr190 of *Tb*PRMT1 ENZ by steric clashes (Fig. 4e). *Tb*PRMT1 PRO, but not ENZ, was found in stress granules, where it would not be accessible for *Tb*PRMT1 ENZ translated in the cytosol, implying that sequestration of *Tb*PRMT1 PRO may provide a means of controlling *Tb*PRMT1 ENZ activity. We propose that *Tb*PRMT1 PRO serves as a folding chaperone for its catalytic partner, providing a new paradigm for prozyme function. Thus, the expression and localization of *Tb*PRMT1 PRO are ultimately determinants of *Tb*PRMT1 ENZ activity.

Analogous folding chaperones have recently been described for *Tb*RNase III enzymes within the RNA editing machinery of *T. brucei* [32], supporting the paradigm for prozyme function in this organism. However, a more detailed comparison between these systems must further await biochemical and structural studies of the editosome complexes. With respect to the other two well-characterized prozymes in *T. brucei*, the folding chaperone function of *Tb*PRMT1 PRO is distinct from AdoMet decarboxylase (*Tb*AdoMetDC) PRO, which serves as an allosteric activator for *Tb*AdoMetDC ENZ [29], and from deoxyhypusine synthase (*Tb*DHS) PRO, which activates *Tb*DHS ENZ by direct active-site complementation [31].

While the former ENZ-PRO system also utilizes AdoMet as a substrate, the fold as well as the AdoMet binding mode of AdoMetDCs are unrelated to those of PRMTs [47, 48].

PRMT1 prozyme function has thus far not been well studied in other related protozoan parasites. Sequence alignments of ENZ and PRO with homologs from related protozoan kinetoplastids (Supplemental Figs. S1 and S2) including the human parasites *T. cruzi* causing Chagas disease and *Leishmania spp*. causing various forms of leishmaniasis suggest that PRMT1 ENZ-PRO complexes also exist in many other parasites and corroborate numerous features and conclusions that we present here for *Tb*PRMT1. Among the putative *Tb*PRMT1 PRO homologs, AdoMet binding residues are not conserved, and the residues forming the η2 3_{10}-helix are missing, consistent with catalytically inactive *Tb*PRMT1 PRO. Furthermore, dimerization residues of *Tb*PRMT1 ENZ and PRO are vastly conserved, indicating the same heterodimer formation in other kinetoplastids. Specifically, Tyr190 of *Tb*PRMT1 ENZ is invariant, arguing that the PRMT1 ENZ proteins of other species are similarly incapable of homodimerization because of steric clashes and that they therefore necessitate a prozyme for stability. Intriguingly, tetrameric interface residues are largely conserved as well, which provides further evidence that heterotetramers are the active species and a prerequisite for methylation. Finally, the first 40 N-terminal *Tb*PRMT1 PRO residues are not conserved, which coincides with our finding that this region is dispensable for substrate binding, while the adjacent residues 41–52 are conserved and critical for substrate recognition. In *Tb*PRMT1 ENZ, the N-terminal residues 1–15 are not conserved and not sufficient for substrate binding. Among the kinetoplastid PRMTs, the enzyme-prozyme paradigm only exists for PRMT1, while *Tb*PRMT5, *Tb*PRMT6 [49], and *Tb*PRMT7 [9, 10] do not have such prozymes for regulation.

From an evolutionary standpoint, we speculate that PRMT1 ENZ and PRO have co-evolved to furnish a functional PRMT1 enzyme, as a mutation in PRMT1 ENZ such as Cys190-to-Tyr would render PRMT1 ENZ unstable, unless PRMT1 PRO concomitantly emerged to function as a folding chaperone for PRMT1 ENZ. Initially, PRMT1 PRO may have been catalytically active, but over time, mutations of the PRMT1 PRO AdoMet binding site may have transformed PRMT1 PRO into a catalytically dead enzyme, focusing on its primary role as a regulator of PRMT1 ENZ. Even if the AdoMet binding residues were not mutated, lack of η2 3_{10}-helix alone may have compromised AdoMet binding within the Rossmann fold. The fact that PRMT1 ENZ-PRO complexes are conserved throughout kinetoplastids suggests that this regulatory mechanism proved to be valuable to these organisms and may constitute a general mechanism of PRMT regulation beyond kinetoplastids.

Materials and Methods

Protein expression and purification

DNA fragments of *Tb*PRMT1 PRO (TriTrypDB: **Tb927.10.3560**) and *Tb*PRMT1 ENZ (TriTrypDB: **Tb927.1.4690**) were amplified by PCR from genomic DNA and cloned into the multiple coning sites (MCS) 1 and 2 using the *Nco*I/*Not*I and *Nde*I/*Xho*I restriction sites of a modified pETDuet-1 vector (Novagen) containing an N-terminal PreScission protease (GE Healthcare) cleavable His_6-tag prior to MCS 1. The constructs were overexpressed in *E. coli* BL21-CodonPlus(DE3)-RIL cells (Stratagene) and grown in LB media containing

appropriate antibiotics. Mutations in ENZ and PRO were introduced by overlap extension PCR mutagenesis. Protein expression was induced at OD_{600} of ≈0.4 with 0.1 mM isopropyl-β-D-thiogalactoside at 18 °C for 16 h. The cells were harvested by centrifugation at 7,500 × *g* and 4°C and lysed with a cell disrupter (Avestin) in a buffer containing 20 mM Tris, pH 8.0, 300 mM NaCl, 5 mM β-mercaptoethanol, 0.5 mM 4-(2-aminoethyl)benzenesulfonyl fluoride hydrochloride (Sigma), 2 mM bovine lung aprotinin (Sigma), and complete EDTA-free protease inhibitor cocktail (Roche). After centrifugation at 35,000 × *g* for 45 min, the cleared lysate was loaded onto a Ni-NTA column (Qiagen) and eluted with an imidazole gradient. Protein-containing fractions were pooled, dialyzed against a buffer containing 20 mM Tris, pH 8.0, 100 mM NaCl, and 5 mM dithiothreitol (DTT), and subjected to cleavage with PreScission protease (GE Healthcare) for 5 h at 4°C. Following His_6-tag removal, the cleaved protein was bound to a heparin column (GE Healthcare) and eluted with a NaCl gradient. Protein-containing fractions were pooled, concentrated, and purified on a HiLoad Superdex 200 16/60 gel filtration column (GE Healthcare) in a buffer containing 20 mM HEPES, pH 7.5, 150 mM NaCl, and 0.5 mM Tris(2-carboxyethyl)phosphine hydrochloride (TCEP).

MBP-tagged *Tb*RGG1 was cloned into a pMAL-c2X vector (NEB) using *Bam*HI and *Sal*I restriction sites. *Tb*RGG1 was overexpressed in *E. coli* BL21-CodonPlus(DE3)-RIL cells (Stratagene) and grown in LB media containing appropriate antibiotics. Protein expression was induced at OD_{600} of ≈0.4 with 0.1 mM isopropyl-β-D-thiogalactoside at 18 °C for 16 h. The cells were harvested by centrifugation at 7,500 × *g* and 4°C and lysed with a cell disrupter (Avestin) in a buffer containing 20 mM Tris, pH 8.0, 300 mM NaCl, 5 mM β-mercaptoethanol, 0.5 mM 4-(2-aminoethyl)benzenesulfonyl fluoride hydrochloride (Sigma), 2 mM bovine lung aprotinin (Sigma), and complete EDTA-free protease inhibitor cocktail (Roche). After centrifugation at 35,000 × *g* for 45 min, the cleared lysate was loaded onto an amylose resin (NEB) and eluted with a maltose gradient. Protein-containing fractions were pooled, dialyzed against a buffer containing 20 mM Tris, pH 7.5, 20 mM NaCl, and 5 mM dithiothreitol (DTT). The protein was bound to a SP column (GE Healthcare) and eluted with a NaCl gradient. Protein-containing fractions were pooled, concentrated, and purified on a HiLoad Superdex 200 16/60 gel filtration column (GE Healthcare) in a buffer containing 20 mM HEPES, pH 7.5, 150 mM NaCl, and 0.5 mM TCEP.

Crystallization, data collection, structure determination and refinement

For formation of the complex with the AdoHcy, 4.5 mg/ml of purified *Tb*PRMT1 ENZ-Δ52PRO was mixed in a 1:8 molar ratio with AdoHcy and incubated for 4 h on ice. The crystallization solution consisted of 7% PEG 4000 and 0.1 M Tris, pH 7.4. Crystals grew in space group C2 at room temperature within a week. X-ray diffraction data were collected at the 24ID-C beamline at the NE-CAT at the Advanced Photon Source (APS) of Argonne National Laboratory (ANL). Diffraction data were processed in HKL2000 [50]. The structure was solved by the single anomalous dispersion (SAD) phasing technique in the program AutoSol of the PHENIX package [51], using data obtained from seleno-L-methionine-labeled crystals. The asymmetric unit contained one tetramer. Model building was performed in O [52] and Coot [53]. The final model spanning residues 21–240 and 251–345 of ENZ and residues 71–389 of PRO was refined in Phenix [51] to an R_{free} of 22.3 %

with excellent stereochemistry as assessed by MolProbity [54]. Details for data collection and refinement statistics are summarized in Supplemental Table S1. Figures were generated using PyMOL (Schrödinger, LLC), the electrostatic potential was calculated with APBS [55]. Atomic coordinates and structure factors have been deposited with the Protein Data Bank under PDB: **6DNZ**.

Multi-angle light scattering

Purified proteins were characterized by multi-angle light scattering following size-exclusion chromatography [56]. Protein at 50 μM was injected onto a Superdex 200 10/300 GL size-exclusion chromatography column (GE Healthcare) equilibrated in a buffer containing 20 mM HEPES pH 7.5, 150 mM NaCl, and 0.5 mM TCEP. The chromatography system was connected in series with an 18-angle light scattering detector (DAWN HELEOS) and refractive index detector (OptilabrEX) (Wyatt Technology). Data were collected every second at a flow rate of 0.25 mL/min at 25 °C. Data analysis was carried out using the program ASTRA, yielding the molar mass and mass distribution (polydispersity) of the sample.

Isothermal titration calorimetry

ITC measurements were performed at 25°C using a MicroCal auto-iTC200 calorimeter (MicroCal, LLC). Wild-type and mutant ENZ-PRO proteins as well as MBP-*Tb*RGG1 protein were extensively dialyzed against a buffer containing 20 mM HEPES, pH 7.5, 150 mM NaCl, and 0.5 mM TCEP. 2 μL of 0.13 mM MBP-*Tb*RGG1 was injected into 0.2 mL of 0.03 mM ENZ-PRO proteins in the chamber every 150 s. Baseline-corrected data were analyzed with ORIGIN software.

Methylation assays

To assay the activity of *Tb*PRMT1 tetramerization mutants, 37.5 nM *Tb*PRMT1 tetramer was mixed with 6 μM MBP-*Tb*RGG1 substrate, 0.7 μM [^{3}H]AdoMet (Adenosyl-L-Methionine, S-[methyl-^{3}H]-, 55–85Ci (2.03–3.15TBq)/mmol; PerkinElmer), 9.3 μM unlabeled AdoMet, 2 mM DTT and 2mM PMSF in PBS in a total volume of 25 μl. Reactions were incubated at 26°C for 1.5 hour, stopped by addition of SDS loading dye and separated on SDS PAGE. Gels were Coomassie stained and soaked in EN^{3}HANCE (PerkinElmer). Dried gels were then exposed to film for one week at −80°C. To assay the activity of *Tb*PRMT1 containing N-terminal prozyme truncations, reactions were performed as above, except the amount of MBP-*Tb*RGG1 substrate was lowered to 0.6 μM, unlabeled AdoMet was left out and 6 μg of MBP2* protein (NEB) was added to each reaction to increase molecular crowding.

Small-Angle X-ray Scattering

SEC–SAXS of wild-type and mutant *Tb*PRMT1 ENZ-PRO proteins was performed at the G1 station at MacCHESS, which is equipped with an ÄKTA Pure FPLC system (GE Healthcare). Protein was loaded at concentrations ranging from 2 to 16 mg/ml on a Superdex 200 10/300 GL column (GE Healthcare) equilibrated in 20 mM HEPES, pH 7.5, 150 mM NaCl, and 0.5 mM TCEP. SAXS data were recorded on a Pilatus 100 K-S detector at 2 s per

frame with a fixed camera length of 1.522 m and an energy of 9.91 keV, allowing the collection of the angular range q of 0.01–0.30 $Å^{-1}$. Primary reduction of the SAXS data was performed using RAW [57]. A Guinier plot of the buffer-subtracted profile was linear to the lowest measured q value. GNOM [58] was used to calculate $P(r)$ plots from the scattering data. The maximum diameter was chosen so that the $P(r)$ function fell gradually to zero at $r = D_{max}$ unconstrained. Theoretical radii of gyration were calculated using CRYSOL [42]. SEC–SAXS data collection and analysis statistics are listed in Table 2.

Electron Microscopy

Negative stain transmission electron microscopy was performed on the wild-type *Tb*PRMT1 ENZ-PRO complex and the *Tb*PRMT1 PRO triple mutant Y215A/M219A/E223A. Samples at 0.03 mg/ml were stained using 2% uranyl formate on continuous carbon grids. Micrographs were collected on the JEOL-1230 transmission electron microscope with a Gatan US400 detector. Data were processed using the Appion pipeline and ISAC [59, 60]. Using Appion, a contrast transfer function estimation was performed using CTFFIND4 [61]. Automated particle picking was done using DoG Picker and FindEM [62]. An initial stack of particles was assembled in Appion. 2D Classification was performed in ISAC [60].

Accession numbers:

The x-ray structure (coordinates and structure files) of the *Tb*PRMT1 ENZ-Δ52PRO complex with AdoHcy have been deposited in the PDB with accession number **6DNZ**.

Supplementary Material

Refer to Web version on PubMed Central for supplementary material.

Acknowledgements

We thank David King (University of California, Berkeley) for mass spectrometry analysis, Igor Kourinov and Kay Perry for support during data collection at NE-CAT, Richard Gillilan for support during data collection at CHESS, the High-Throughput Screening and Spectroscopy Resource Center at Rockefeller University, and the X-Ray Crystallography & Molecular Characterization Facility at the Sidney Kimmel Cancer Center, which is supported in part by National Cancer Institute Cancer Center Support Grant P30 CA56036 and S10 OD017987. X-ray data were collected at the NE-CAT beamlines (GM103403) on a Pilatus detector (RR029205) at the APS (DE-AC02-06CH11357). CHESS is supported by the NSF award DMR-1332208, and the MacCHESS resource is supported by NIGMS award GM-103485. The electron microscopy work was performed at the Simons Electron Microscopy Center and National Resource for Automated Molecular Microscopy located at the New York Structural Biology Center, supported by grants from the Simons Foundation (SF349247), NYSTAR, and the NIH National Institute of General Medical Sciences (GM103310). This work was supported by National Institutes of Health Grant R01 AI060260 (to L. K. R.) and American Heart Association Predoctoral Fellowship 15PRE24480155 (to L. K.). We would like to thank the members of the Debler laboratory for helpful discussions and the reviewers for constructive criticism.

Abbreviations used

ADMA	asymmetric dimethyl arginine
AdoMet	S-Adenosyl-L-methionine
AdoHcy	S-Adenosyl-L-homocysteine
ENZ	*Tb*PRMT1 enzyme

ITC	isothermal titration calorimetry
MMA	monomethyl arginine
PRMT	protein arginine methyltransferase
PRO	*Tb*PRMT1 prozyme
rmsd	root-mean-square deviation
SDMA	symmetric dimethyl arginine

References

[1]. Keating J, Yukich JO, Sutherland CS, Woods G, Tediosi F. Human African trypanosomiasis prevention, treatment and control costs: a systematic review. Acta Trop. 2015;150:4–13. [PubMed: 26056739]

[2]. Gibson WC, Swinkels BW, Borst P. Post-transcriptional control of the differential expression of phosphoglycerate kinase genes in Trypanosoma brucei. J Mol Biol. 1988;201:315–25. [PubMed: 2458474]

[3]. Clayton CE. Gene expression in Kinetoplastids. Curr Opin Microbiol. 2016;32:46–51. [PubMed: 27177350]

[4]. Schulz D, Mugnier MR, Paulsen EM, Kim HS, Chung CW, Tough DF, et al. Bromodomain Proteins Contribute to Maintenance of Bloodstream Form Stage Identity in the African Trypanosome. PLoS Biol. 2015;13:e1002316. [PubMed: 26646171]

[5]. Gary JD, Clarke S. RNA and protein interactions modulated by protein arginine methylation. Prog Nucleic Acid Res Mol Biol. 1998;61:65–131. [PubMed: 9752719]

[6]. Lott K, Li J, Fisk JC, Wang H, Aletta JM, Qu J, et al. Global proteomic analysis in trypanosomes reveals unique proteins and conserved cellular processes impacted by arginine methylation. J Proteomics. 2013;91:210–25. [PubMed: 23872088]

[7]. Thandapani P, O'Connor TR, Bailey TL, Richard S. Defining the RGG/RG motif. Mol Cell. 2013;50:613–23. [PubMed: 23746349]

[8]. Cheng X, Collins RE, Zhang X. Structural and sequence motifs of protein (histone) methylation enzymes. Annu Rev Biophys Biomol Struct. 2005;34:267–94. [PubMed: 15869391]

[9]. Jain K, Warmack RA, Debler EW, Hadjikyriacou A, Stavropoulos P, Clarke SG. Protein Arginine Methyltransferase Product Specificity Is Mediated by Distinct Active-site Architectures. J Biol Chem. 2016;291:18299–308. [PubMed: 27387499]

[10]. Debler EW, Jain K, Warmack RA, Feng Y, Clarke SG, Blobel G, et al. A glutamate/aspartate switch controls product specificity in a protein arginine methyltransferase. Proc Natl Acad Sci U S A. 2016;113:2068–73. [PubMed: 26858449]

[11]. Fuhrmann J, Clancy KW, Thompson PR. Chemical biology of protein arginine modifications in epigenetic regulation. Chem Rev. 2015;115:5413–61. [PubMed: 25970731]

[12]. Goulah CC, Pelletier M, Read LK. Arginine methylation regulates mitochondrial gene expression in Trypanosoma brucei through multiple effector proteins. RNA. 2006;12:1545–55. [PubMed: 16775306]

[13]. Pelletier M, Pasternack DA, Read LK. In vitro and in vivo analysis of the major type I protein arginine methyltransferase from Trypanosoma brucei. Mol Biochem Parasitol. 2005;144:206–17. [PubMed: 16198009]

[14]. Kafkova L, Debler EW, Fisk JC, Jain K, Clarke SG, Read LK. The Major Protein Arginine Methyltransferase in Trypanosoma brucei Functions as an Enzyme-Prozyme Complex. J Biol Chem. 2017;292:2089–100. [PubMed: 27998975]

[15]. Kafková L, Tu C, Pazzo KL, Smith KP, Debler EW, Paul KS, Qu J, Read LK. 2018 Trypanosoma brucei PRMT1 is a nucleic acid binding protein with a role in energy metabolism and the starvation stress response. mBio 9:e02430–18. 10.1128/mBio.02430-18.

[16]. Goulah CC, Read LK. Differential effects of arginine methylation on RBP16 mRNA binding, guide RNA (gRNA) binding, and gRNA-containing ribonucleoprotein complex (gRNP) formation. J Biol Chem. 2007;282:7181–90. [PubMed: 17229732]

[17]. Zhang X, Cheng X. Structure of the predominant protein arginine methyltransferase PRMT1 and analysis of its binding to substrate peptides. Structure. 2003;11:509–20. [PubMed: 12737817]

[18]. Zhang X, Zhou L, Cheng X. Crystal structure of the conserved core of protein arginine methyltransferase PRMT3. EMBO J. 2000;19:3509–19. [PubMed: 10899106]

[19]. Weiss VH, McBride AE, Soriano MA, Filman DJ, Silver PA, Hogle JM. The structure and oligomerization of the yeast arginine methyltransferase, Hmt1. Nat Struct Biol. 2000;7:1165–71. [PubMed: 11101900]

[20]. Tang J, Frankel A, Cook RJ, Kim S, Paik WK, Williams KR, et al. PRMT1 is the predominant type I protein arginine methyltransferase in mammalian cells. J Biol Chem. 2000;275:7723–30. [PubMed: 10713084]

[21]. Wang H, Huang ZQ, Xia L, Feng Q, Erdjument-Bromage H, Strahl BD, et al. Methylation of histone H4 at arginine 3 facilitating transcriptional activation by nuclear hormone receptor. Science. 2001;293:853–7. [PubMed: 11387442]

[22]. Tang J, Gary JD, Clarke S, Herschman HR. PRMT 3, a type I protein arginine N-methyltransferase that differs from PRMT1 in its oligomerization, subcellular localization, substrate specificity, and regulation. J Biol Chem. 1998;273:16935–45. [PubMed: 9642256]

[23]. Siegel TN, Hekstra DR, Wang X, Dewell S, Cross GA. Genome-wide analysis of mRNA abundance in two life-cycle stages of Trypanosoma brucei and identification of splicing and polyadenylation sites. Nucleic Acids Res. 2010;38:4946–57. [PubMed: 20385579]

[24]. Kolev NG, Franklin JB, Carmi S, Shi H, Michaeli S, Tschudi C. The transcriptome of the human pathogen Trypanosoma brucei at single-nucleotide resolution. PLoS Pathog. 2010;6:e1001090. [PubMed: 20838601]

[25]. Albanes D, Brown C. Relative weight, height and risk of breast cancer. JAMA. 1990;263:3148.

[26]. Shimogawa MM, Saada EA, Vashisht AA, Barshop WD, Wohlschlegel JA, Hill KL. Cell Surface Proteomics Provides Insight into Stage-Specific Remodeling of the Host-Parasite Interface in Trypanosoma brucei. Mol Cell Proteomics. 2015;14:1977–88. [PubMed: 25963835]

[27]. Lott K, Zhu L, Fisk JC, Tomasello DL, Read LK. Functional interplay between protein arginine methyltransferases in Trypanosoma brucei. Microbiologyopen. 2014;3:595–609. [PubMed: 25044453]

[28]. Willert E, Phillips MA. Regulation and function of polyamines in African trypanosomes. Trends Parasitol. 2012;28:66–72. [PubMed: 22192816]

[29]. Volkov OA, Kinch L, Ariagno C, Deng X, Zhong S, Grishin N, et al. Relief of autoinhibition by conformational switch explains enzyme activation by a catalytically dead paralog. Elife. 2016;5.

[30]. Nguyen S, Jones DC, Wyllie S, Fairlamb AH, Phillips MA. Allosteric activation of trypanosomatid deoxyhypusine synthase by a catalytically dead paralog. J Biol Chem. 2013;288:15256–67. [PubMed: 23525104]

[31]. Afanador GA, Tomchick DR, Phillips MA. Trypanosomatid Deoxyhypusine Synthase Activity Is Dependent on Shared Active-Site Complementation between Pseudoenzyme Paralogs. Structure. 2018;26:1499–512 e5. [PubMed: 30197036]

[32]. McDermott SM, Carnes J, Stuart K. Editosome RNase III domain interactions are essential for editing and differ between life cycle stages in Trypanosoma brucei. RNA. 2019;25:1150–63. [PubMed: 31171708]

[33]. Pils B, Schultz J. Inactive enzyme-homologues find new function in regulatory processes. J Mol Biol. 2004;340:399–404. [PubMed: 15210342]

[34]. Murphy JM, Mace PD, Eyers PA. Live and let die: insights into pseudoenzyme mechanisms from structure. Curr Opin Struct Biol. 2017;47:95–104. [PubMed: 28787627]

[35]. Rossmann MG, Moras D, Olsen KW. Chemical and biological evolution of nucleotide-binding protein. Nature. 1974;250:194–9. [PubMed: 4368490]

[36]. Cheng X, Roberts RJ. AdoMet-dependent methylation, DNA methyltransferases and base flipping. Nucleic Acids Res. 2001;29:3784–95. [PubMed: 11557810]

[37]. FAUMAN EB, BLUMENTHAL RM, CHENG X. STRUCTURE AND EVOLUTION OF ADOMET-DEPENDENT METHYLTRANSFERASES. S-Adenosylmethionine-Dependent Methyltransferases: WORLD SCIENTIFIC; 2011 p. 1–38.

[38]. Rambo RP, Tainer JA. Accurate assessment of mass, models and resolution by small-angle scattering. Nature. 2013;496:477–81. [PubMed: 23619693]

[39]. Pawlak MR, Banik-Maiti S, Pietenpol JA, Ruley HE. Protein arginine methyltransferase I: substrate specificity and role in hnRNP assembly. J Cell Biochem. 2002;87:394–407. [PubMed: 12397599]

[40]. Goulet I, Gauvin G, Boisvenue S, Cote J. Alternative splicing yields protein arginine methyltransferase 1 isoforms with distinct activity, substrate specificity, and subcellular localization. J Biol Chem. 2007;282:33009–21. [PubMed: 17848568]

[41]. Yue WW, Hassler M, Roe SM, Thompson-Vale V, Pearl LH. Insights into histone code syntax from structural and biochemical studies of CARM1 methyltransferase. EMBO J. 2007;26:4402–12. [PubMed: 17882261]

[42]. Svergun D, Barberato C, Koch MHJ. CRYSOL - a Program to Evaluate X-ray Solution Scattering of Biological Macromolecules from Atomic Coordinates. Journal of Applied Crystallography. 1995;28:768–73.

[43]. Antonysamy S, Bonday Z, Campbell RM, Doyle B, Druzina Z, Gheyi T, et al. Crystal structure of the human PRMT5:MEP50 complex. Proc Natl Acad Sci U S A. 2012;109:17960–5. [PubMed: 23071334]

[44]. Rho J, Choi S, Seong YR, Cho WK, Kim SH, Im DS. Prmt5, which forms distinct homo-oligomers, is a member of the protein-arginine methyltransferase family. J Biol Chem. 2001;276:11393–401. [PubMed: 11152681]

[45]. Eyers PA, Murphy JM. The evolving world of pseudoenzymes: proteins, prejudice and zombies. BMC Biol. 2016;14:98. [PubMed: 27835992]

[46]. Lijnzaad P, Argos P. Hydrophobic patches on protein subunit interfaces: characteristics and prediction. Proteins. 1997;28:333–43. [PubMed: 9223180]

[47]. Ekstrom JL, Mathews II, Stanley BA, Pegg AE, Ealick SE. The crystal structure of human S-adenosylmethionine decarboxylase at 2.25 A resolution reveals a novel fold. Structure. 1999;7:583–95. [PubMed: 10378277]

[48]. Tolbert WD, Ekstrom JL, Mathews II, Secrist JA 3rd, Kapoor P, Pegg AE, et al. The structural basis for substrate specificity and inhibition of human S-adenosylmethionine decarboxylase. Biochemistry. 2001;40:9484–94. [PubMed: 11583147]

[49]. Wang C, Zhu Y, Chen J, Li X, Peng J, Chen J, et al. Crystal structure of arginine methyltransferase 6 from Trypanosoma brucei. PLoS One. 2014;9:e87267. [PubMed: 24498306]

[50]. Otwinowski Z, Minor W. Processing of X-Ray Diffraction Data Collected in Oscillation Mode. Methods Enzymol. 1997;276:307–26.

[51]. Adams PD, Afonine PV, Bunkóczi G, Chen VB, Echols N, Headd JJ, et al. The Phenix software for automated determination of macromolecular structures. Methods. 2011;55:94–106. [PubMed: 21821126]

[52]. Jones TA, Zou J-Y, Cowan SW, Kjeldgaard M. Improved methods for building protein models in electron density maps and the location of errors in these models. Acta Crystallogr A. 1991;47:110–9. [PubMed: 2025413]

[53]. Emsley P, Lohkamp B, Scott WG, Cowtan K. Features and development of Coot. Acta crystallographica Section D, Biological crystallography. 2010;66:486–501. [PubMed: 20383002]

[54]. Davis IW, Leaver-Fay A, Chen VB, Block JN, Kapral GJ, Wang X, et al. MolProbity: all-atom contacts and structure validation for proteins and nucleic acids. Nucleic acids research. 2007;35:W375–83. [PubMed: 17452350]

[55]. Baker NA, Sept D, Joseph S, Holst MJ, McCammon JA. Electrostatics of nanosystems: application to microtubules and the ribosome. Proceedings of the National Academy of Sciences of the United States of America. 2001;98:10037–41. [PubMed: 11517324]

[56]. Wyatt PJ. Multiangle light scattering: The basic tool for macromolecular characterization. Instrum Sci Technol. 1997;25:1–18.

[57]. Hopkins JB, Gillilan RE, Skou S. BioXTAS RAW: improvements to a free open-source program for small-angle X-ray scattering data reduction and analysis. J Appl Crystallogr. 2017;50:1545–53. [PubMed: 29021737]

[58]. Svergun DI, Semenyuk AV, Feigin LA. Small-angle-scattering-data treatment by the regularization method. Acta Crystallogr. A 1988;44:244–250.

[59]. Lander GC, Stagg SM, Voss NR, Cheng A, Fellmann D, Pulokas J, et al. Appion: an integrated, database-driven pipeline to facilitate EM image processing. J Struct Biol. 2009;166:95–102. [PubMed: 19263523]

[60]. Yang Z, Fang J, Chittuluru J, Asturias FJ, Penczek PA. Iterative stable alignment and clustering of 2D transmission electron microscope images. Structure. 2012;20:237–47. [PubMed: 22325773]

[61]. Rohou A, Grigorieff N. CTFFIND4: Fast and accurate defocus estimation from electron micrographs. J Struct Biol. 2015;192:216–21. [PubMed: 26278980]

[62]. Voss NR, Yoshioka CK, Radermacher M, Potter CS, Carragher B. DoG Picker and TiltPicker: software tools to facilitate particle selection in single particle electron microscopy. J Struct Biol. 2009;166:205–13. [PubMed: 19374019]

Highlights

- The crystal structure of *Trypanosoma brucei* protein arginine methyltransferase 1 (PRMT1) is reported
- Two enzyme-prozyme heterodimers form a stable heterotetramer essential for catalysis
- The catalytically dead prozyme lacks elements essential for AdoMet binding
- The enzyme alone is unstable and cannot form a canonical dimer due to steric clashes
- *T. brucei* PRMT1 prozyme adopts a chaperone function conserved across kinetoplastids

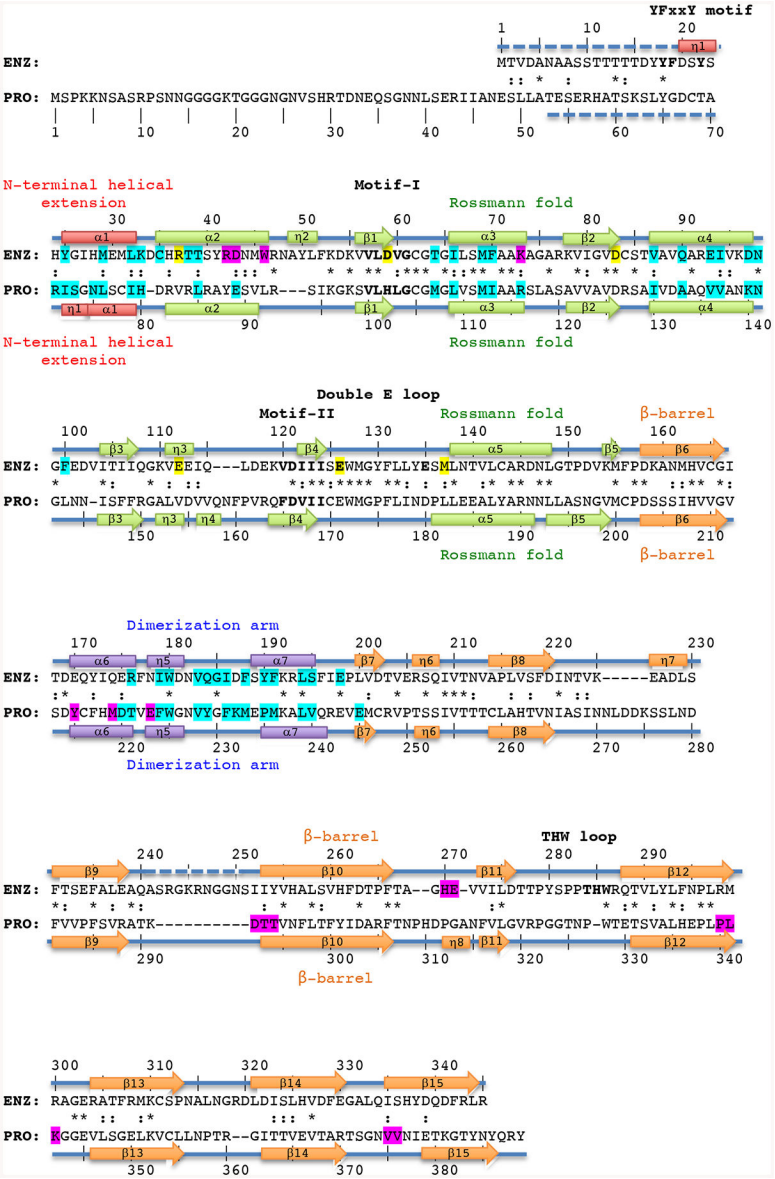

Figure 1. Structure-based sequence alignment of *Tb*PRMT1 enzyme and prozyme

Structure-based alignment of *Tb*PRMT1 enzyme (ENZ) and *Tb*PRMT1 prozyme (PRO). α1-α7 refer to α-helices, η1-η8 to 3_{10}-helices, and β1-β15 to β-strands, indicating the secondary structure elements of *Tb*PRMT1 ENZ and PRO. Residue numbering is shown above (ENZ) and below (PRO) the sequences. Red designates the N-terminal helical extension (ENZ residues 20–33, PRO residues 71–80), green the Rossmann fold (ENZ residues 34–157, and PRO residues 81–202), orange the β-barrel (ENZ residues 158–345, and PRO residues 203–389), and purple the dimerization arm (ENZ residues 168–199, and PRO residues 213–244). Similar and identical residues are marked as : and *, respectively. Residues highlighted in magenta are involved in tetramer formation, and residues highlighted in cyan are involved in ENZ-PRO dimer formation. Signature residues of the YFxxY motif, Motif-I, -II, the double E-loop, and the THW-loop are shown in bold. Key

AdoMet-binding residues of ENZ are highlighted in yellow. Disordered regions are represented by dashed lines.

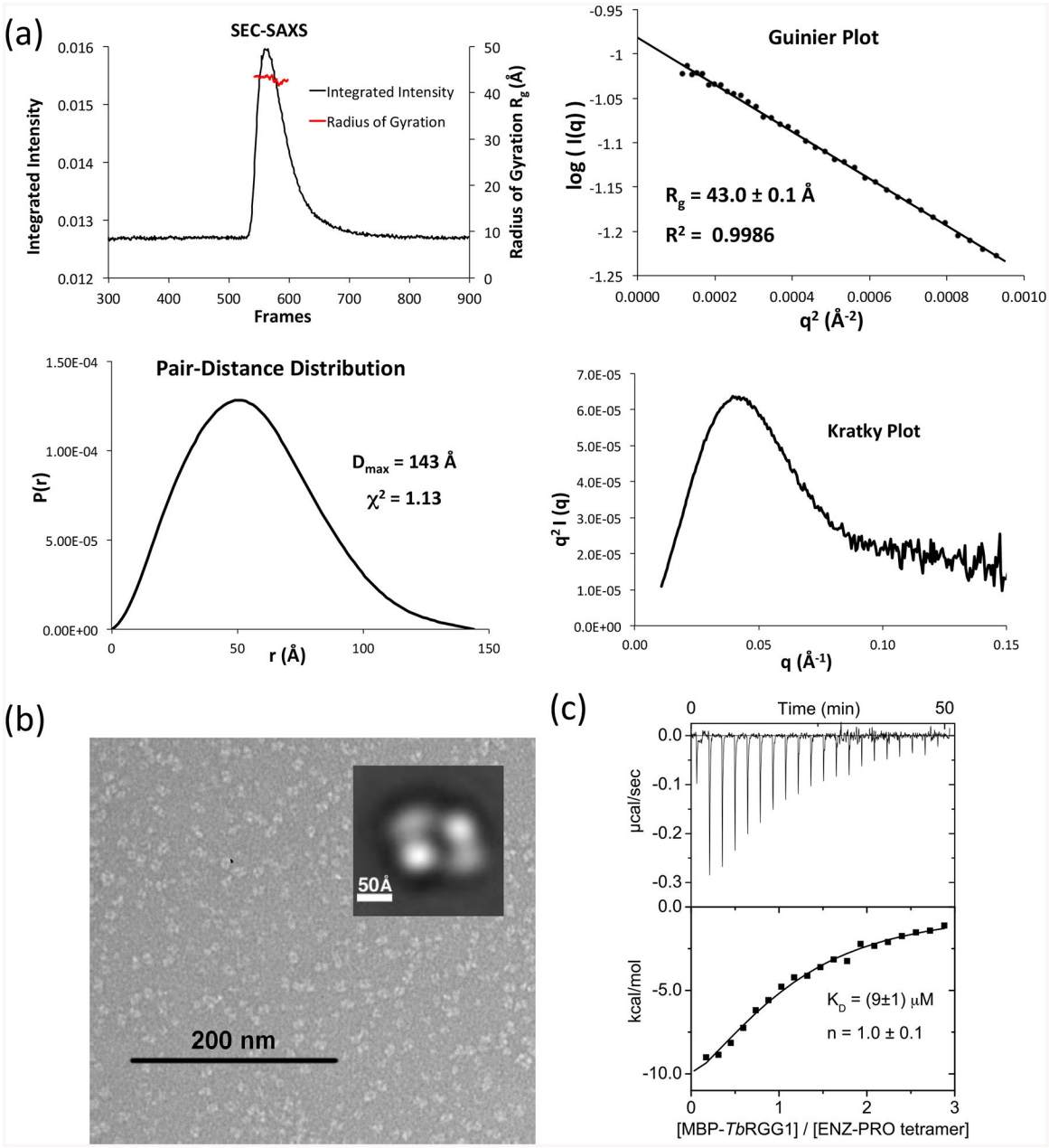

Figure 2. *Tb*PRMT1 ENZ-PRO forms a heterotetrameric complex in solution

(a) SEC–SAXS analysis of *Tb*PRMT1 ENZ-PRO. Top left panel: SEC-SAXS integrated intensities (left y-axis) plotted against frame number (x-axis). The red dots indicate radius of gyration, R_g (on the right y-axis). Top right panel: Guinier plot calculated from averaging buffer-subtracted scattering intensities. The coefficient of determination, R^2, is 0.9986. Bottom left panel: Pair-distance distribution function P(r), yielding a maximum molecular diameter of 143 Å. Bottom right panel: Normalized Kratky plot calculated from SEC–SAXS data.

(b) Negative-stain electron microsopy. EM micrograph with a 200 nm scale bar. Inset: Predominant 2D class average.

(c) ITC thermogram (upper panel) and plot of corrected heat values (lower panel) for binding of the heterotetrameric *Tb*PRMT1 ENZ-PRO complex to Maltose Binding Protein (MBP)-fused *Tb*RGG1 protein.

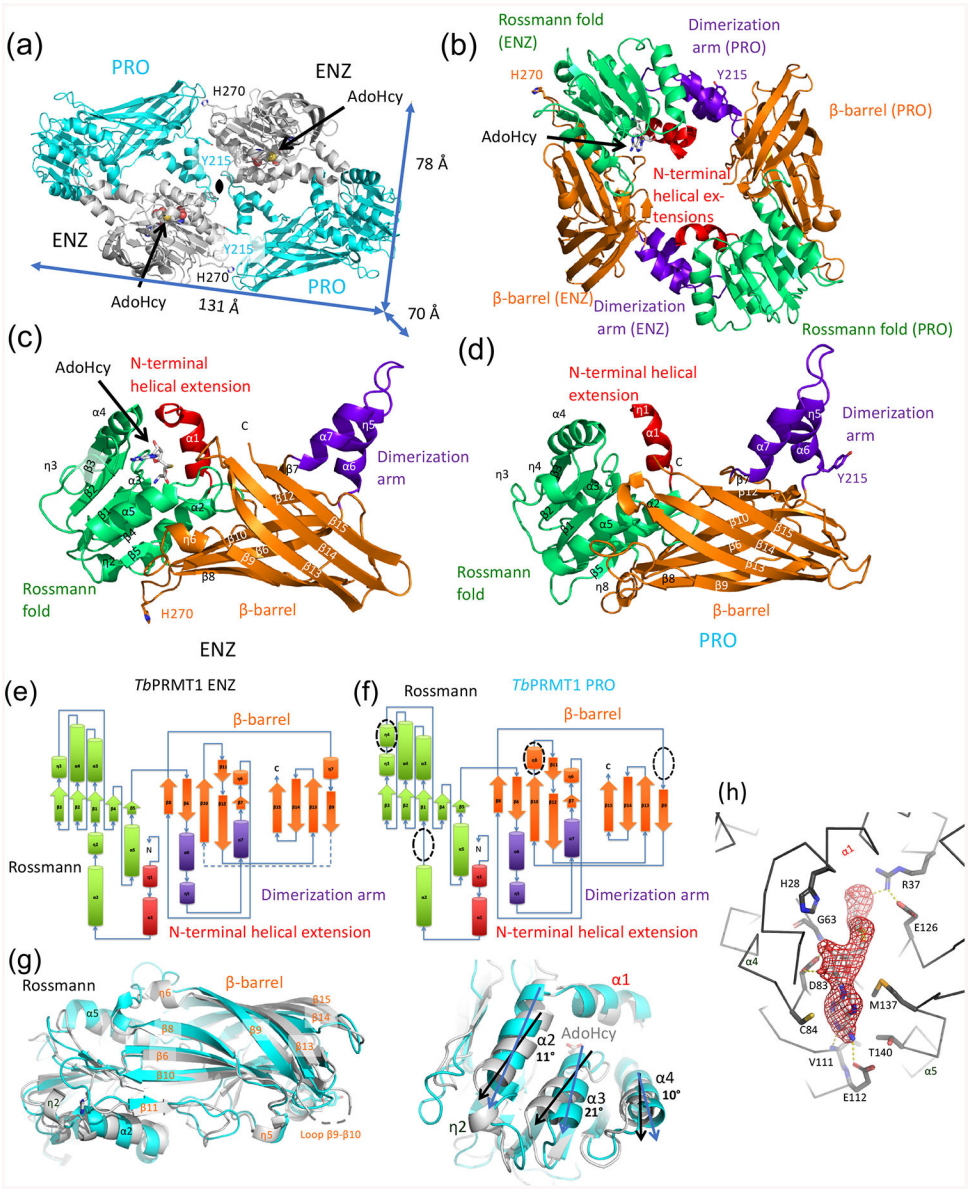

Figure 3. Crystal structure of the heterotetrameric *Tb*PRMT1 ENZ-PRO complex

(a) Tetrameric *Tb*PRMT1 ENZ-PRO complex. One *Tb*PRMT1 ENZ (gray) bound to AdoHcy shown in space-filling representation forms a heterodimer with *Tb*PRMT1 PRO (cyan). The dimensions of the tetrameric complex are shown. The non-crystallographic twofold symmetry axis is shown as a black pointed oval. Key residues involving tetramerization (His270 of ENZ, and Tyr215 of PRO) are indicated.

(b) Anti-parallel *Tb*PRMT1 ENZ-PRO heterodimer. The N-terminal helical extension (red), the Rossmann fold (green), the β-barrel (orange) and the dimerization arm (purple) are shown. AdoHcy, His270, and Tyr215 are highlighted.

(c) Monomeric *Tb*PRMT1 ENZ structure.

(d) Monomeric *Tb*PRMT1 PRO structure.

(e) Topology of *Tb*PRMT1 ENZ.

(f) Topology of *Tb*PRMT1 PRO.

(g) Superimposition of monomeric *Tb*PRMT1 ENZ and PRO. Left panel: Overall structure. Right panel: Close-up view on Rossmann fold, illustrating rotated α-helices.

(h) Simulated-annealing omit electron density map for AdoHcy, contoured at 3.5σ above the mean.

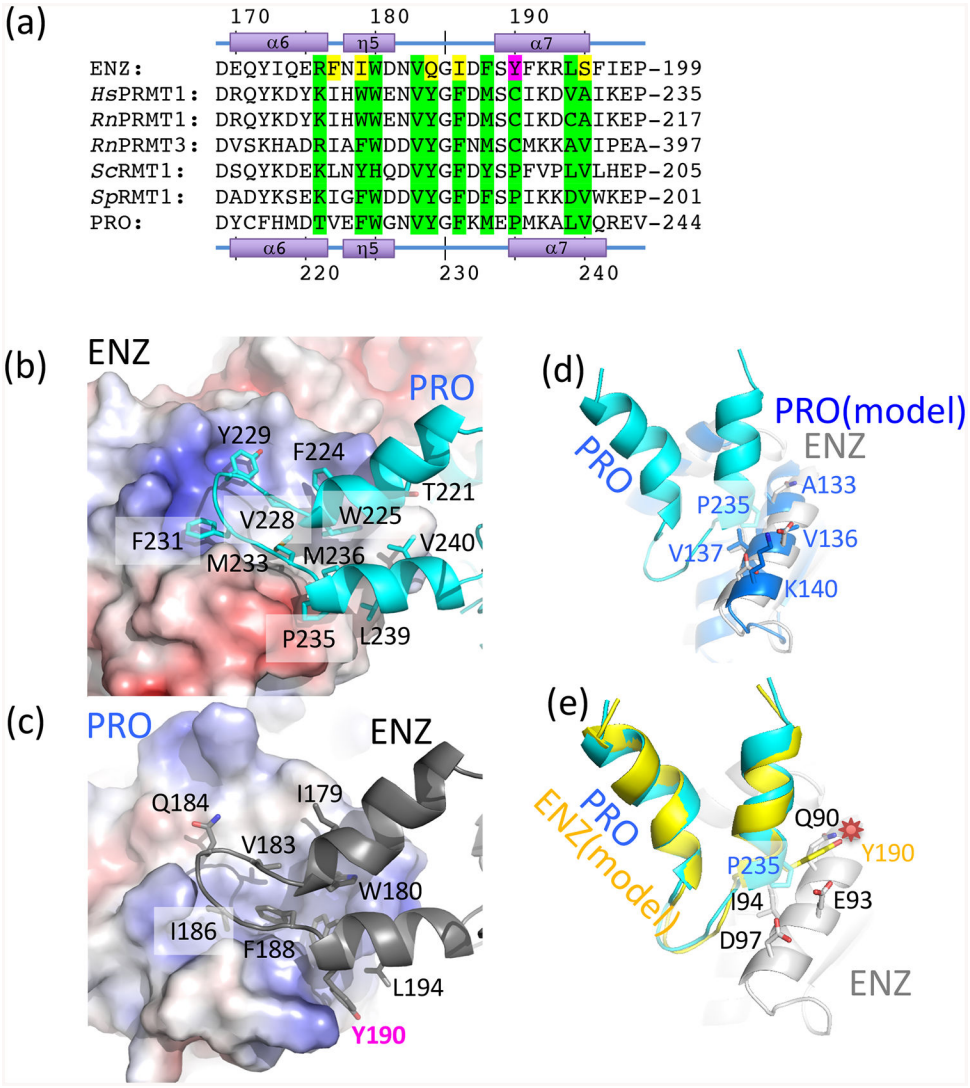

Figure 4. The dimerization arm of *Tb*PRMT1 ENZ features non-conserved residues, preventing *Tb*PRMT1 ENZ homodimerization

(a) Sequence alignment of the dimerization arm regions of *Tb*PRMT1 ENZ (TriTrypDB ID: Tb927.1.4690), rat PRMT1 (GenBank ID: NP_077339), rat PRMT3 (NP_446009), budding yeast RMT1 (NP_009590), fission yeast RMT1 (NP_594825), and *Tb*PRMT1 PRO (TriTrypDB ID: Tb927.10.3560). Conserved interface residues are colored in green. Non-conserved interface residues are colored in yellow. The non-conserved *Tb*PRMT1 ENZ Tyr190 is highlighted in magenta.

(b) Hydrophobic interaction of the *Tb*PRMT1 PRO dimerization arm with the *Tb*PRMT1 ENZ Rossmann fold.

(c) Hydrophobic interaction of the *Tb*PRMT1 ENZ dimerization arm with the *Tb*PRMT1 PRO Rossmann fold.

(d) Modelled *Tb*PRMT1 PRO-PRO interface.

(e) Modelled *Tb*PRMT1 ENZ-ENZ interface. The non-conserved Tyr190 causes a steric clash between two *Tb*PRMT1 ENZ molecules highlighted by a red star, which interferes with dimerization.

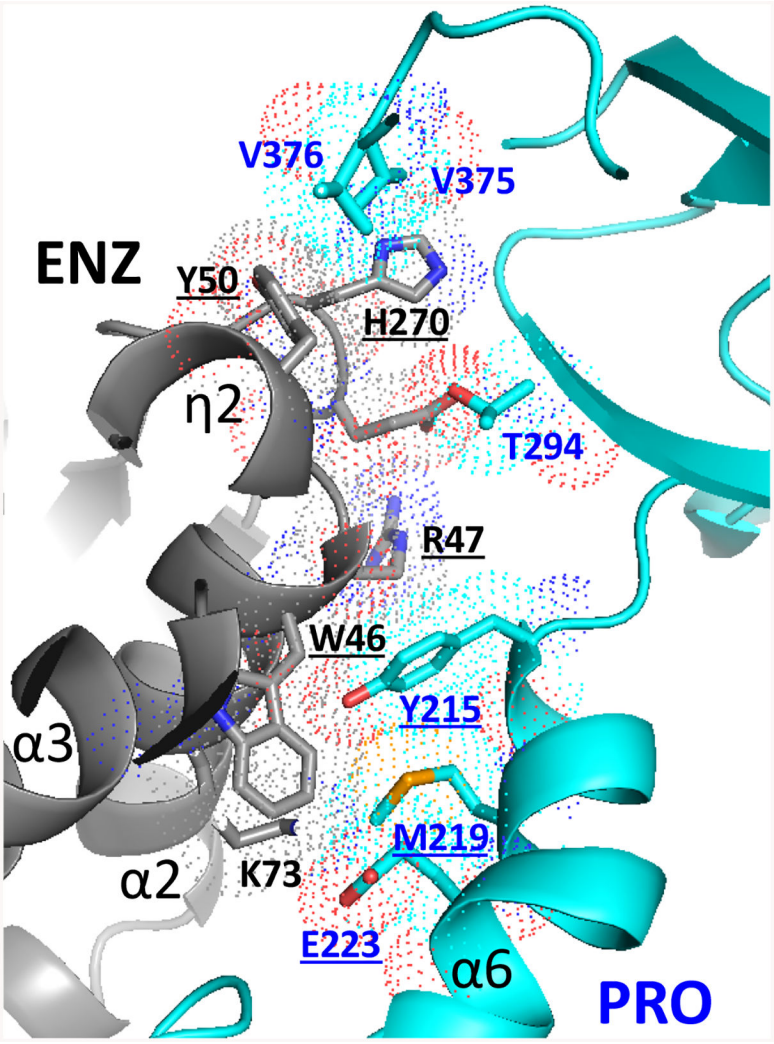

Figure 5. The interface between two *Tb*PRMT1 ENZ-PRO heterodimers is dominated by van der Waals' contacts.

Residues forming key contacts between two *Tb*PRMT1 ENZ-PRO heterodimers are displayed in dotted-sphere representation, indicating their van der Waals' radii. Mutation of the underlined residues breaks the heterotetrameric assembly into *Tb*PRMT1 ENZ-PRO heterodimers.

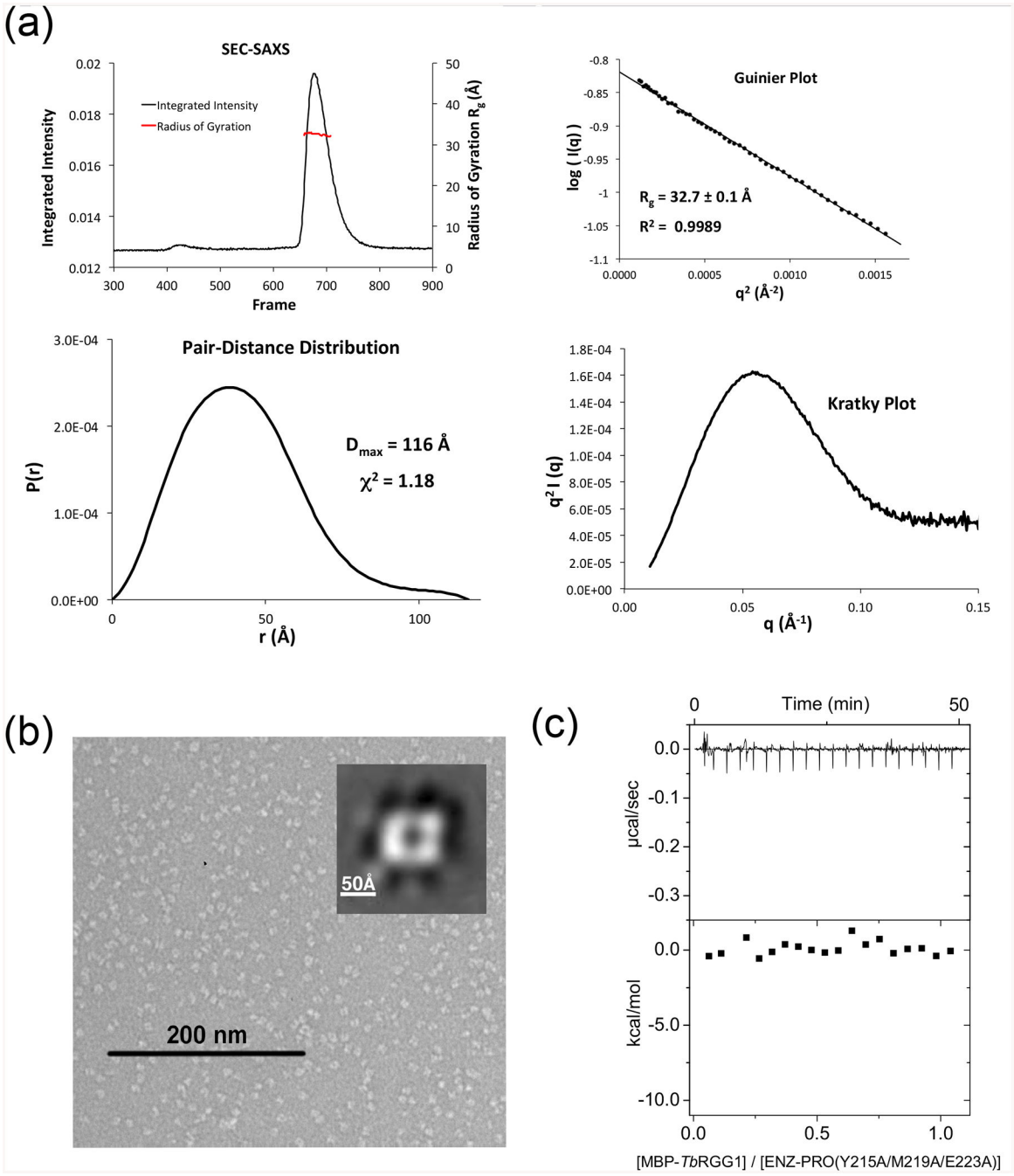

Figure 6. Structure-based mutagenesis of the tetrameric interface yields stable *Tb*PRMT1 ENZ-PRO heterodimers

(a) SEC–SAXS analysis of a representative heterodimeric *Tb*PRMT1 ENZ-PRO mutant (the ENZ W46A/R47A/Y50A triple mutant). Top left panel: SEC-SAXS integrated intensities (left y-axis) plotted against frame number (x-axis). The red dots indicate radius of gyration, R_g (on the right y-axis). Top right panel: Guinier plot calculated from averaging buffer-subtracted scattering intensities. The coefficient of determination, R^2, is 0.9989. Bottom left panel: Pair-distance distribution function P(r), yielding a maximum molecular diameter of 116 Å. Bottom right panel: Normalized Kratky plot calculated from SEC–SAXS data.

(b) Negative-stain electron microscopy analysis of a representative *Tb*PRMT1 ENZ-PRO mutant (the PRO Y215A/M219A/E223A triple mutant). EM micrograph with a 200 nm scale bar. Inset: Predominant 2D class average.
(c) ITC thermogram (upper panel) and plot of corrected heat values (lower panel) for binding of the *Tb*PRMT1 ENZ Y215A/M219A/E223A triple mutant to Maltose Binding Protein (MBP)-fused *Tb*RGG1 protein.

Table 1.

Methyltransferase activities, molecular weight, and binding affinities of *Tb*PRMT1 ENZ-PRO and truncated *Tb*PRMT1 PRO mutants

ENZ (1–345)	PRO (1–389)	Expression	Solubility	MALS (kDa)	Methyltransferase activity	MBP-*Tb*RGG1 binding (μM)
full-length	full-length	+++/+++	+++/++++	164	+++	9±1[a]
full-length	Δ11	+++/+++	+++/++++	162	+++	n.d.[b]
full-length	Δ21	+++/+++	+++/++++	165	+++	36±8
full-length	Δ31	+++/+++	+++/++++	171	+++	86±10
full-length	Δ41	+++/+++	+++/++++	160	+++	n.d.[b]
full-length	Δ45	+++/+++	+++/++++	n.d.[b]	+	160±20
full-length	Δ52	+++/+++	+++/++++	157	-	no binding
full-length	-	+++	not soluble			

[a]The standard deviations were calculated from two or three independent measurements

[b]not determined

Table 2.

SEC-SAXS analysis of ENZ-PRO wild-type, ENZ-Δ52PRO, and interface mutants

ENZ	**WT**	**WT**	**W46A/R47A/ Y50A**	**WT**	**WT**	**WT**	**H270A**
PRO	**WT**	**Δ52**	**WT**	**Y215A/M219A**	**Y215A/M219A/ E223A**	**Y215A/ T294A**	**Y215A**
instrument	G1 beamline						
wavelength (Å)	1.25						
exposure time (s)	1						
temperature (K)	277						
protein concentration (mg/ml)	3.8/8.0	1.5/4.0/8.0	2.3/3.2	3.0	3.0/16	6.0/12.0	6.0/16.0
radius of gyration R_g[a,b] (Å)	42.9±0.2	40.9±0.6	32.1±0.7	33.4±0.1	32.6±0.2	32.0±0.1	32.1±0.3
maximum diameter, D_{max}[b]	143±2	138±4	116±7	120	118±3	117±2	118±4
M.W.[b,c] (kDa)	187±2	166±9	84.7±0.7	88.3	83±3	84.1±0.8	82.6±0.8
theoretical M.W.[d] (kDa)	163.2	152.8	81.3	81.5	81.3	81.5	81.5

[a] R_g determined from a Guinier plot.

[b] The standard deviations were calculated from two or three independent measurements except for the ENZ(WT)/PRO(Y215A/M219A) mutant, where the error corresponds to the fitting error of the Guinier plot.

[c] The M.W. was derived from the volume of correlation V_C [33].

[d] The theoretical M.W. refers to a heterotetramer for the wild-type and the ENZ-Δ52PRO version and to a heterodimer for the mutants.

Table 3.

Methyltransferase activity, molecular weight, and MBP-*Tb*RGG1 binding affinities of ENZ-PRO and tetrameric interface mutants

ENZ (1–345)	PRO (1–389)	Expression	Solubility	MALS (kDa)	SEC elution volume (mL)	Methyl-transferase activity	MBP-*Tb*RGG1 Binding (μM)
full-length	full-length	+++/+++	+++/+++	164	68	+++	9±1[a]
K73A	full-length	+++/+++	+++/+++	164	68	n.d.	n.d.[b]
H270A, E271A	full-length	+++/+++	+++/+++	142	71	+++	n.d.
W46A	full-length	+++/+++	+++/+++	167	67	n.d.	n.d.
R47A	full-length	+++/+++	+++/+++	162	69	n.d.	n.d.
Y50A	full-length	+++/+++	+++/+++	152	69	n.d.	n.d.
H270A	full-length	+++/+++	+++/+++	149	69	n.d.	n.d.
W46A, R47A, Y50A	full-length	+++/+++	+++/+++	80	80	-	no binding
Y50A, H270A	full-length	+++/+++	+++/+++	89	74	-	n.d.
full-length	Y215A	+++/+++	+++/+++	107	70	+	n.d.
full-length	K232A	+++/+++	+++/+++	165	68	n.d.	n.d.
full-length	Y215A, M219A	+++/+++	+++/+++	84	76	-	no binding
full-length	Y215A, M219A, E223A	+++/+++	+++/+++	81	79	-	no binding
full-length	Y215A, E223A	+++/+++	+++/+++	84	77	-	no binding
full-length	Y215A, K232A	+++/+++	+++/+++	90	75	-	n.d.
full-length	Y215A, T294A	+++/+++	+++/+++	81	79	-	no binding
H270A	Y215A	+++/+++	+++/+++	80	79	-	no binding

[a]The standard deviations were calculated from two or three independent measurements

[b]not determined